PHYSICAL REVIEW B **95**, 064424 (2017)

Elucidation of the helical spin structure of FeAs

T. Frawley,[1] R. Schoonmaker,[1] S. H. Lee,[2] C.-H. Du,[2] P. Steadman,[3] J. Strempfer,[4] Kh. A. Ziq,[5] S. J. Clark,[1] T. Lancaster,[1] and P. D. Hatton[1]

[1]*Durham University, Department of Physics, South Road, Durham, DH1 3LE, United Kingdom*

[2]*Physics Department, Tamkang University, Tamsui 251, Taiwan*

[3]*Diamond Light Source, Harwell Science and Innovation Campus, Didcot, Oxon, OX11 ODE*

[4]*DESY Photon Science, Notkestrasse 85, 22607, Hamburg, Germany*

[5]*King Fahd University of Petroleum and Minerals, Department of Physics, Dhahran 31261, Saudi Arabia*

(Received 26 October 2016; published 22 February 2017)

We present the results of resonant x-ray scattering measurements and electronic structure calculations on the monoarsenide FeAs. We elucidate details of the magnetic structure, showing the ratio of ellipticity of the spin helix is larger than previously thought, at 2.58(3), and reveal both a right-handed chirality and an out-of-plane component of the magnetic moments in the spin helix. We find that electronic structure calculations and analysis of the spin-orbit interaction are able to qualitatively account for this canting.

DOI: 10.1103/PhysRevB.95.064424

I. INTRODUCTION

Unlike the cuprates, where the magnetic state owes its existence to Mott insulator physics, in iron-based superconductors magnetism results from an instability of the delocalized Fe d-band electrons, which gives rise to a spin-density wave [1–5]. The pnictide parent compounds display metallic, antiferromagnetic spin-density wave ground states where the spins are periodically modulated in space but where the outermost electrons can be delocalized, typical of the collective effect that emerges from an instability of the paramagnetic Fermi surface. A key question remains how the parent magnetic state in pnictides evolves across the phase diagram and how the properties of the doped magnet can compete, promote, or coexist with superconductivity. The simplest of all iron arsenide systems, the monoarsenide FeAs, may provide some insights into these questions since, it has been argued [6], its itinerant magnetism is related to the magnetic ground states of iron-based superconductors.

FeAs crystallizes in the B31 (MnP-type) structure (space group $Pnma$) [7], which consists of distorted $FeAs_6$ octahedra, which are face sharing along the a axis and edge sharing along the b and c axes (Fig. 1). It therefore has similar Fe-Fe linkages to the layered Fe-based superconductors (such as LaFeAsO, $BaFe_2As_2$, and NaFeAs), but is distinguished from them by being surrounded by six (octahedral) rather than four (tetrahedral) arsenic atoms. The iron atoms sit at the *4c* Wyckoff site, giving rise to four positions in the unit cell: Fe_1 at [6] $(x, \frac{1}{4}, z)$, Fe_2 at $(\bar{x}+\frac{1}{2}, \frac{3}{4}, z+\frac{1}{2})$, Fe_3 at $(\bar{x}, \frac{3}{4}, \bar{z})$, and Fe_4 at $(x+\frac{1}{2}, \frac{1}{4}, \bar{z}+\frac{1}{2})$, where $x = 0.004$ and $z = 0.199$ as shown in Fig. 2.

Initial neutron powder diffraction measurements [8] showed that FeAs undergoes a transition to a long-range antiferromagnetically ordered state at $T_N = 77$ K. It was suggested that the system adopts a helical magnetic structure with a wave vector $q = [0,0,0.375]$ and an ordered magnetic moment of 0.5 μ_B. However, a more recent magnetic susceptibility and transport study [9] gave results that indicated the presence of significant magnetocrystalline anisotropy, raising doubts about the occurrence of such a simple spin helix structure. Specifically, single crystal susceptibility shows a kink at 70 K in the a and b directions but not in the c direction. (The lack of features in the c-axis direction suggesting the magnetic moment is fixed in the a-b plane.) The key observation is that the susceptibility along the b axis is lower than that along a, and only the b axis displays a magnetic field splitting, suggesting the presence of anisotropy. Following this, a polarized single-crystal neutron diffraction study [6] suggested a slightly elliptical helical structure comprising a noncollinear spin-density wave arising from a combination of itinerant and localized behavior, with the spin amplitude along the b-axis direction being 1.5(5)% larger than that along the a direction.

In terms of its electronic properties, FeAs lies between two well-understood regimes: the delocalized magnetic metal and the localized magnetic insulator. Resistivity measurements [9] confirm the itinerant behavior of FeAs: resistivity decreases below 150 K with a kink observed at 70 K. Electronic structure calculations on FeAs have not fully elucidated the mechanism that generates the magnetic structure. Nonpolarized, collinear, and noncollinear spin calculations have been carried out, but find the lowest energy state to be antiferromagnetic, in which nearest-neighbor iron spins antialign with a resultant $P2_1/m$ symmetry [5,11,12]. The study by Parker and Mazin [5] calculated the static Lindhard function in FeAs and the nesting of the Fermi surface in the AFM phase, and concluded that some form of nesting did not drive the magnetic order. Griffin and Spaldin [11] compared the use of different DFT functionals in FeAs and found that GGA-hybrid GGA gives values for the structure in closest agreement with experiment, but that a negative Hubbard-U calculation would be most likely to reproduce the spin spiral as it would increase competition between AFM and FM interactions and increase the energy of the AFM state. However, there is no other physical justification for a negative Hubbard-U parameter, implying a larger failing in these functionals. Griffin and Spaldin also performed noncollinear spin calculations imposing a variety of spirals on the system but found that the AFM state was lower in energy than all of them.

In this paper we present a refinement of the magnetic structure of iron arsenide using x-ray resonant elastic scattering (XRES) and calculations of the electronic structure using

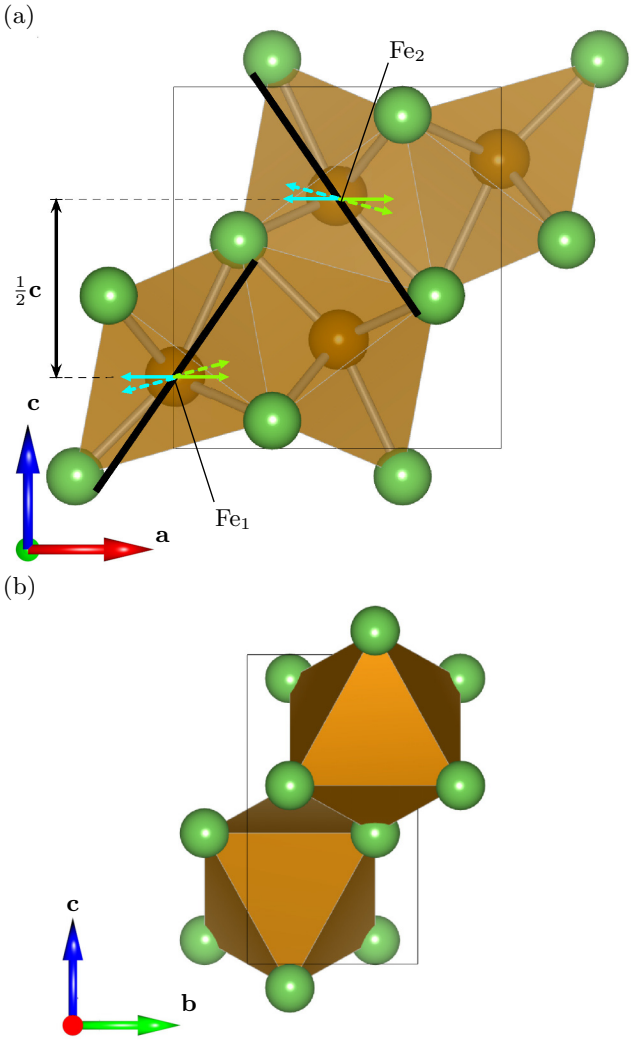

FIG. 1. Crystal structure of FeAs in (a) the *a*-*c* plane; and (b) the *b*-*c* plane. (As atoms denoted by green circles.)

density functional theory (DFT). From analysis of a magnetic satellite reflection, our XRES results strongly suggest that the magnetic spiral is considerably more elliptical than was previously believed, has a right-handed chirality, and has an ordered spin component in the propagation direction of the helix. DFT calculations show that spin-orbit interactions and the local iron environment provide an explanation for this new ordering component. We conclude that the spin ordering is linked to localized orbital restructuring and changes in electronic density, and therefore, as might be expected, is not well described by simple Stoner or Ising-type models.

II. EXPERIMENTAL AND COMPUTATIONAL METHODS

Our sample of FeAs was grown by an iodine vapor transport method [13]. The growth method resulted in single crystals of typical dimensions ≈100 μm. Several samples were characterized using a four-circle diffractometer, and a single

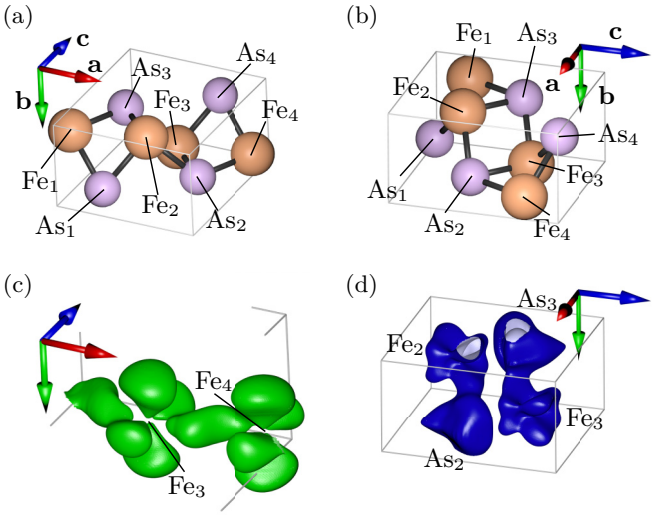

FIG. 2. (a, b) Crystal structure of FeAs showing the different Fe atoms. Selected regions of (c) electron density decrease and (d) density increase on change from zero-spin to AFM1 calculated states.

crystal selected, with a natural *c*-axis facet and a sharp [0,0,2] reflection with a rocking width of just 0.0025°.

XRES measurements were carried out at both the soft Fe $L_{\mathrm{II/III}}$ and the hard Fe *K* absorption edges. For the Fe *L* edges experiments the beamlines ID08 (at ESRF) and I10 (at Diamond) were used. For the *K* edge experiments the beamline P09 (at Petra III) was used. All three beamlines are situated on an undulator insertion device. For the ID08 and I10 experiments the sample was mounted with the *b* axis in the scatter plane. For the P09 experiment the [−1,0,0] reciprocal direction was used as the azimuthal reference vector.

DFT calculations were run with the CASTEP electronic structure code using the PBE exchange-correlation functional [14,15]. Energy differences between spin configurations were converged to 1 part in 10 000, and to generate the Fermi-surface a Monkhorst-Pack *k*-point grid of 23 × 27 × 19 was used. To account for core state contributions on atoms an ultrasoft core-corrected iron pseudopotential with 8 valence electrons and an arsenic pseudopotential with 15 valence electrons were used. A nonmagnetic configuration and a range of collinear ordered spin-structures were considered.

III. X-RAY SCATTERING RESULTS

A. Soft x-ray scattering

At the Fe L_{III} energy (≈707 eV) the radius of the Ewald sphere limits access along the *l* reciprocal direction to $l = 0.68$. Within this limit two resonant reflections were found at positions $l = 0.389$ and $l = 0.611$. A scan along the [00*L*] direction is shown in Fig. 3. The observed peaks are asymmetric (most likely due to the energy profile of the undulator), with the peak at $l = 0.611$ having the reverse asymmetry to the $l = 0.389$ reflection. This suggests that [0,0,0.611] is a satellite of the forbidden [0,0,1] Bragg peak. The two reflections can be indexed as $[0,0,0] + [0,0,\tau]$ (denoted τ hereafter) and $[0,0,1] - [0,0,\tau]$ (denoted $1 - \tau$ hereafter), where $\tau = 0.389$. Energy resonances of the two

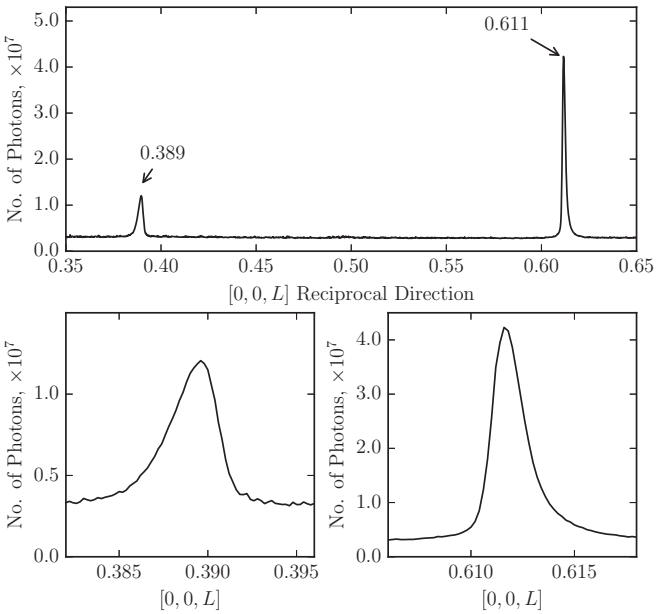

FIG. 3. Scan along the L reciprocal lattice direction, at the Fe L_{III} edge. Due to the large wavelength of the Fe L_{III} edge, the Ewald sphere is limited to $0.68c^*$.

reflections, without post-scatter polarization analysis (Fig. 4), were performed by decreasing the energy of the incident x-ray while maintaining the diffraction condition for the magnetic peak. The resonances were measured with both σ- and π-polarized incident light. Assuming a dipole-dipole transition ($E1E1$) is responsible for the resonant feature, the transition is from the Fe $2p$ orbital to the Fe $3d$ band. Exciting into this Fe $3d$ band leads to the sensitivity of the technique to the local magnetism, as it is the $3d$ orbitals that are the

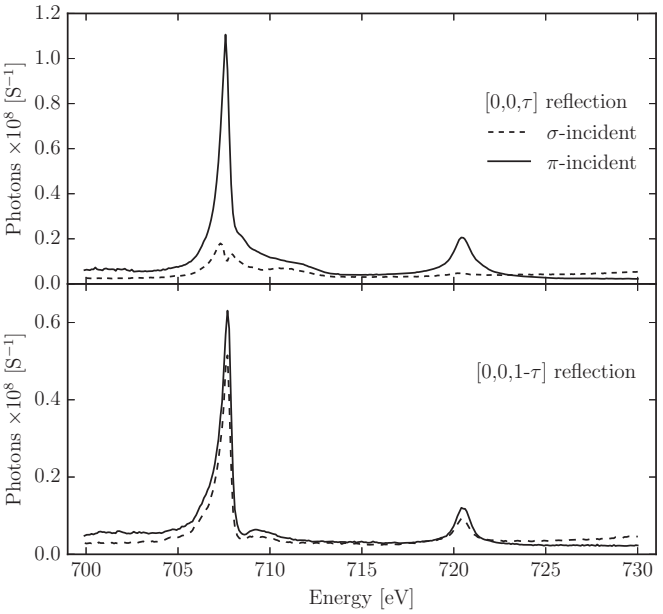

FIG. 4. Energy resonance of the magnetic satellite peaks, $[0,0,\tau]$ (top) and $[0,0,1-\tau]$ (bottom), with σ- and π-polarized incident light. No post-scatter polarization analysis was used.

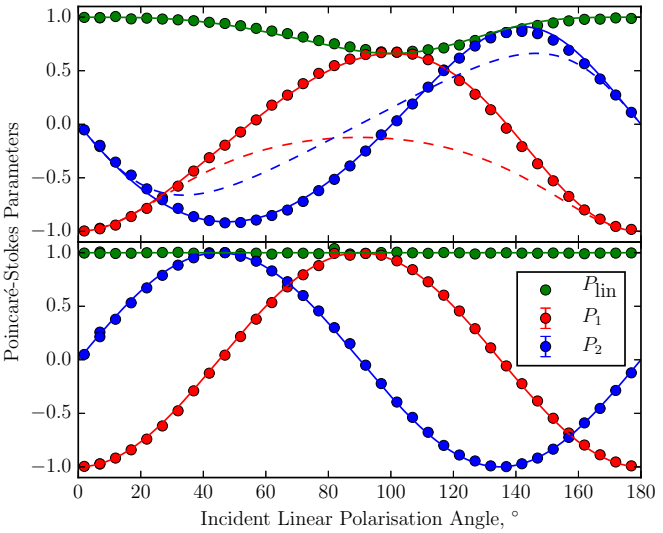

FIG. 5. Full linear polarization analysis (FLPA). Top: FLPA measured on the $[0,0,\tau]$ reflection. Bottom: FLPA measured on the $[0,0,1-\tau]$ reflection. The solid lines are the elliptical helix model based on the derived structure factor. The dashed lines are the predictions for a circular helix discussed in Sec. IV C.

magnetically active spin-polarized band in iron. We also note that the temperature behavior of the $[0,0,\tau]$ magnetic Bragg peak shows critical behavior consistent with that observed previously [6].

The τ reflection shows a marked difference between the two polarization channels, which is sufficient to rule out either charge scattering or simple collinear magnetic spin structures along the a, b, or c directions, assuming a $E1E1$ origin to the scattering. The $1-\tau$ reflection shows very different behavior, giving equal intensity with incident σ- and π-polarized light (Fig. 4). This indicates a different origin for the two peaks. The τ and $1-\tau$ reflections occur at θ angles of 34.4° and 63.7°, respectively. These angles are not close to 45° or 90°, which might cause a suppression of scattering due to the θ dependencies of the scattering amplitude. For the τ reflection the intensity in the circular-positive channel is roughly twice that of the circular-negative channel, indicative of a noncollinear spin structure. The $1-\tau$ reflection has equal intensity in the circular-positive and circular-negative channels. This again shows very different behavior to the τ peak.

A full linear polarization analysis (FLPA) was also carried out on both peaks using the ultra-high vacuum diffractometer, RASOR at I10, and the results are shown in Fig. 5. In this measurement the incident linear light is rotated through a full 180°, and at each incident polarization angle, the polarization state of the scattered beam is measured. Figure 5 shows the incident polarization angle against the outgoing polarization using Poincaré-Stokes parameters, P_1 and P_2. The results show a different polarization analysis for the τ and $1-\tau$ reflections, confirming they have different origins.

B. Hard x-ray scattering

XRES measurents at the hard x-ray energy of the Fe K absorption edge allow for a wider field of access to reciprocal

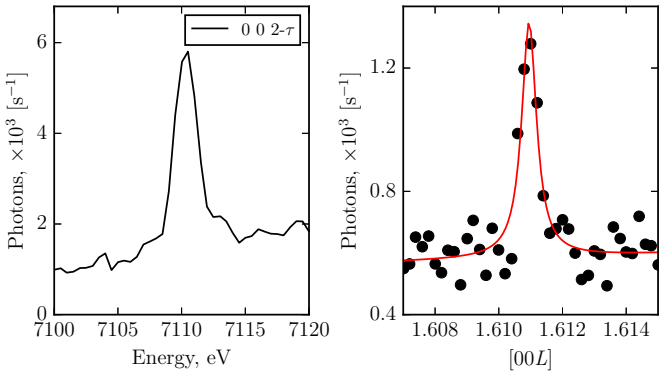

FIG. 6. Left: energy scan of resonance of the $[0,0,2-\tau]$ magnetic reflection. Right: $[00L]$ Reciprocal space scan of $[0,0,2-\tau]$. Scans were performed in the $\sigma-\pi$ channel.

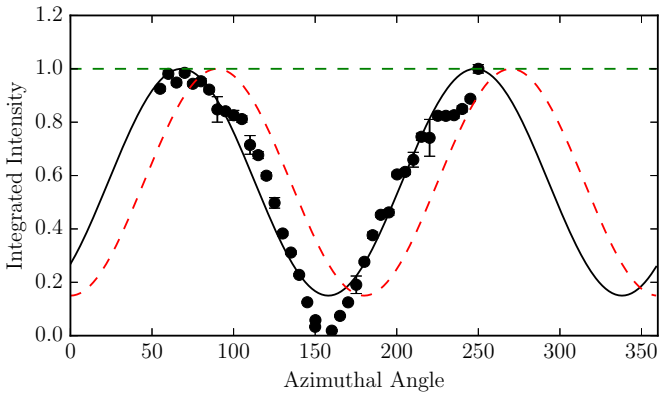

FIG. 7. Azimuthal measurement of the $[0,0,2-\tau]$ magnetic Bragg peak. The dashed and solid lines show predictions made using the structure factor. The green dashed line shows the expected azimuth for circular helical magnetic structure. The red dashed line shows the expected azimuth for a elliptical helical magnetic structure ($m_a : m_b = 1 : 2.58$). The solid black line shows the prediction for the elliptical helix rotated by -22°.

space than measurements at the soft energies, but at a cost of sensitivity to the magnetism. A typical $E1E1$ transition at the Fe K absorption edge excites a Fe $1s$ electron into the empty Fe $4p$ band. The sensitivity to magnetism arises from any overlap, or hybridization, between the Fe $3d$ and Fe $4p$ bands.

A survey of resonant reflections was carried out and satellite reflections were found at $[0,0,2-\tau]$, $[0,0,2+\tau]$, $[0,0,4-\tau]$, $[0,0,4+\tau]$, as well as at $[0,0,2\tau]$ and $[0,0,3\tau]$. An off-axis reflection was also observed at the $[1,0,3-\tau]$ position. No reflections were found at positions away from the odd forbidden Bragg peaks ($[0,0,1\pm\tau]$ and $[0,0,3\pm\tau]$). Figure 6 shows the resonances and reciprocal space scans of the $[0,0,2-\tau]$ peak. All types of satellite reflection show a sharp resonant feature at 7110 eV. The reciprocal space scans show the $[0,0,2-\tau]$ peak to be the sharpest with a width of 0.0006(1) r.l.u., while the 2τ and 3τ reflections are wider with widths of 0.0019(1) and 0.0014(1) r.l.u., respectively. The τ and 2τ reflections were found only in the $\sigma-\pi$ channel and not in the $\sigma-\sigma$ channel, while the 3τ reflection was found in both channels but was stronger in the $\sigma-\sigma$ channel. An $E1E1$-type transition can produce τ and 2τ reflections, but a quadrupole-quadrupole-type transition (E2E2, involving an excitation from the $1s$ orbital into the magnetically active $3d$ spin-polarized band) is required to explain the presence of a 3τ reflection.

An azimuthal measurement was performed on the $[0,0,2-\tau]$ reflection (Fig. 7), which involves a rotation of the sample around the scattering vector, maintaining the diffraction condition. The zero point on the azimuthal axis is defined as when the $[-1,0,0]$ reciprocal vector is in the scattering plane away from the incident beam. Qualitatively, these azimuth data rules out a simple nonelliptical helix. For the $[0,0,2-\tau]$ reflection, the scattering vector is parallel to the magnetic propagation direction; an azimuthal measurement rotates around the magnetic propagation vector. If the magnetic helix was circular, then there would be no change in moment direction upon an azimuthal rotation, and constant intensity would be expected.

The observation of not just the $[0,0,\tau]$ but also the $[0,0,2\tau]$ and $[0,0,3\tau]$ reflections is very reminiscent of x-ray scattering studies of chromium metal. Chromium is the canonical example of an itinerant, incommensurate antiferromagnet below its Néel temperature $T_N = 311$ K [16]. This transverse spin-density wave (SDW) is well understood and arises from a nesting effect between the $3d$ electron pocket centered at the Γ point and the hole pocket centered at the edge of the Brillouin zone at the H point. The pairing is between momentum states separated by wave vector Q and a spiral density wave is formed. The ground state is then formed from two spiral waves of opposite helicity resulting in a long period, linearly polarized SDW. Associated with the SDW ordering, there is a distortion of the lattice with twice the wave vector of the SDW, causing a charge-density wave (CDW). This results in differing satellites surrounding the Bragg peaks with odd multiples of Q being magnetic satellites resulting from the SDW and even multiples of Q caused by the CDW. Thus, $\pm Q$ and $\pm 3Q$ magnetic satellites were first observed by neutron diffraction [17] and $\pm 2Q$ and ± 4 charge satellites observed by x-ray scattering [18]. The observation of the fourth harmonic suggests that the CDW is not perfectly sinusoidal. It is not yet clear as to the exact mechanism for producing a density wave in the charge distribution, with both a magnetostriction effect (coupling the elasticity to the magnetism) [19], or a purely electronic effect based on nesting between electronic bands [20], being claimed. This is similar, but slightly different to our observations, suggesting that in FeAs the τ and 2τ satellites are magnetic in character but the 3τ satellite has both magnetic and charge characteristics. Further studies of the temperature dependence of these satellites may help unravel their origin.

IV. MAGNETIC STRUCTURE DETERMINATION

A. The nature of the ellipse

To determine the magnetic structure of the material, we consider an elliptical magnetic helix pointing along the c axis with spin components S_a and S_b in the a and b directions, respectively, and a chirality $\chi(=\pm)$. The magnetic moment on the nth atom in the jth unit cell for a spin helix with

propagation vector $\boldsymbol{\tau}$ is given by

$$\boldsymbol{m}_{n,j}(\boldsymbol{r}_{n,j}) = S_a \cos(\boldsymbol{\tau}\cdot\boldsymbol{r}_{n,j} - \psi_n)\hat{\boldsymbol{a}} \quad (1)$$

$$+ S_b \cos(\boldsymbol{\tau}\cdot\boldsymbol{r}_{n,j} - \psi_n + \chi\pi/2)\hat{\boldsymbol{b}}, \quad (2)$$

where ψ_n is the phase shift caused by the orbit of Fe_n. For such a helix propagating along the $[0,0,L]$ direction, satellite peaks only appear around even Bragg reflections with structure factor

$$f_{00l} \propto (\boldsymbol{\varepsilon}'\times\boldsymbol{\varepsilon})\cdot\mathbf{M}(e^{i2\pi z_1 l}e^{-i\psi_1} + e^{-i2\pi z_1 l}e^{-i\psi_3}) + (\boldsymbol{\varepsilon}'\times\boldsymbol{\varepsilon})\cdot\mathbf{M}^*(e^{i2\pi z_1 l}e^{i\psi_1} + e^{-i2\pi z_1 l}e^{i\psi_3}), \quad (3)$$

where $\boldsymbol{\varepsilon}'\times\boldsymbol{\varepsilon}$ is a polarization factor, $\boldsymbol{M} = S_a\hat{\boldsymbol{a}} + i\chi S_b\hat{\boldsymbol{b}}$, z_1 is the fractional coordinate of Fe_1, and l is a Miller index.

We fit the ellipticity to the FLPA analysis of the $[0,0,\tau]$ reflection in Fig. 5 (top) and the azimuthal measurement of the $[0,0,2-\tau]$ reflection shown in Fig. 7, which shows the predicted azimuthal dependencies for perfectly circular helical structure, and elliptical structures.

A circular structure gives a constant intensity as a function of azimuthal angle, as expected. As the structure is made more elliptical, the azimuth changes from a constant to a sinusoidally changing intensity. If the magnetic structure has the long axis of the ellipse pointing down the b axis, then the azimuth goes through a minimum at 180°. However, we find that the azimuth of the $[0,0,2-\tau]$ reflection goes through a minimum at around 157°. In our magnetization model, the azimuth intensity can only go to zero at 0°and 180° or 90° and 270° depending on whether the long axis of the ellipse is along the a or b axis. To account for this, the ellipse is allowed to rotate such that long- and short-axes no longer point along the a and b axes.

In order to fit the azimuth of the $[0,0,2-\tau]$, the long axis of the ellipse has to be placed along the b axis and rotated by −22°, as shown in Fig. 7. As the magnetic structure is elliptical rather than circular, the form of the FLPA of the $[0,0,\tau]$ should be highly dependent on the azimuth at which the measurement is taken. In the FLPA of the $[0,0,\tau]$ reflection, the rotation of the ellipse has a similar effect to changing the azimuth position at which the calculation is performed. The effect of ellipticity on the FLPA measurement is quite dramatic and is shown in Fig. 5. For example, for a circular magnetic structure, the predicted P_1 remains negative for all incident angles. The FLPA does not require a rotation of the magnetic ellipse to fit the data, but the rotation can be accommodated by correcting for a potential offset in the azimuth position.

Combining both the azimuth of the $[0,0,2-\tau]$ reflection and the FLPA of the $[0,0,\tau]$ reflection allows a fit requiring only three parameters, the ellipticity, S_b/S_a, the rotation, ζ, and the azimuth offset of the polarization analysis measurement ψ_{flpa}. The final fit results in an ellipticity of $\frac{S_b}{S_a} = 2.58 \pm 0.03$, which is far more substantial than the ellipticity of 1.15 proposed by the neutron experiment of Rodriguez *et al.* [6]. The azimuthal measurement suggests a rotation of the ellipse of $-21.9 \pm 0.2°$. (As a consequence the azimuthal position of FLPA needs to be $11.0 \pm 0.2°$. This value of the azimuthal offset from the b-axis is within the experimental uncertainty of mounting the sample.) The differences between our results and those derived from the neutron experiments [6] probably result from the very different techniques used to estimate the magnitude of the ellipticity. The study of Rodriguez *et al.* used the intensity profiles of 16 relatively low-intensity nuclear and magnetic reflections from polarized neutron diffraction measurements. Our study, however, has used the intensity variation of the azimuthal dependence of a resonantly enhanced x-ray magnetic satellite as well as the full linear polarized analysis of a separate magnetic satellite, which were combined and fitted with a model involving just three adjustable parameters.

B. The effect of spin canting

The $[0,0,1-\tau]$ reflection is predicted to have zero intensity from the above structure factor. In order to explain the origin of this reflection, a spin helix along the c axis with moments restricted to lie within the a-b plane is not sufficient. The phase difference brought about by the two-orbit structure is the origin for the predicted extinction of the $[0,0,1-\tau]$ reflection, and not the direction of the magnetization vector. This means that changing the magnetic structure to a cycloid or collinear spin density wave will not change the extinction of $[0,0,1-\tau]$, while the two-orbit structure remains. It is also the case that adding a canting in the c direction will not contribute to a satellite peak as adding a c-axis component to the magnetic moment that oscillates with a periodicity of τ will contribute only to the satellite of allowed Bragg peaks.

If we assume the existence of an easy axis for the magnetic moment tied to the crystal geometry, it is reasonable to assume that this lies in the a-c plane. The black line in Fig. 1 shows an example direction for the easy axis, and the green and blue arrows show the canting effect on the a component of the moment toward the easy axis. For the moments on the Fe_1 and Fe_2 sites that make up one orbit of the helix, the magnetic easy axis on the Fe_2 site will be a reflection by the σ_x mirror plane of the easy axis on site Fe_1, resulting in a canting in the opposite direction along the c axis. The same relationship holds for the canting effects between the Fe_3, Fe_4 sites. As Fe_1 and Fe_2 are half a unit cell apart the oscillation in the c-axis canting can be described by a cosinusoid with a periodicity of the unit cell, with a phase shift between the two orbits, proportional to the difference in the z component of the positions of Fe_1 and Fe_3. The resulting c-axis component of the magnetic moment is dependent on both its position along the c direction in the unit cell and the position around the magnetic helix, as only the a-axis component of the moment experiences a canting effect.

A c-axis component of the jth magnetic moment is given by

$$\boldsymbol{m}_{n,j}(\mathbf{r}_{n,j})\cdot\hat{\mathbf{c}} = \alpha_{a,c}\beta_n S_a \cos(\boldsymbol{\tau}\cdot\mathbf{r}_{n,j} - \psi_n), \quad (4)$$

where $S_a\cos(\boldsymbol{\tau}\cdot\mathbf{r}_{n,j} - \psi_n)$ is the magnitude of the a component of the spin, and $\alpha_{a,c}$ is a constant that is determined by the strength of the canting effect, and β_n takes the value ±1 depending on the atomic site (i.e., Fe_1 and Fe_3 take the value $+1$ and Fe_2 and Fe_4 the value -1). The specific direction of magnetic easy axis is included in the the value β_n. For example, if the easy axis is perpendicular to the example shown in Fig. 1, then $\alpha_{a,c}$ takes a negative value; if the easy axis is entirely along the a or c axis, then $\alpha_{a,c}$ will be zero.

Including the c-axis component in the structure factor allows the simulation of the full polarization analysis

of the $[0,0,1-\tau]$ (solid lines in Fig. 5). The predicted structure factor for the $[0,0,1-\tau]$ is only dependent on the c-axis component of the magnetization vector. There are no parameters to fit in simulating the FLPA, as the only parameter $\alpha_{a,c}$ controls the strength of the tilting, i.e., the magnitude of the c-axis component with respect to the helical component, and consequently has no impact on the polarization dependence of the $[0,0,1-\tau]$. The simulation of the polarization dependence of the $[0,0,1-\tau]$ reflection gives good agreement with a collinear c-axis moment. This confirms the canted model, where only the component of the moment in the c direction experiences a canting effect, and the $Fe_{1,3}$ and $Fe_{2,4}$ sites have opposite canting effects. However, the full polarization analysis of the $[0,0,1-\tau]$ reflection does not contain information about the magnitude of the canting, while the $[0,0,\tau]$ reflection only contains information about the c-axis component. We note that it is therefore not possible to extract the size of the canting from polarization analysis of reflections along the $[0,0,L]$ direction. However, we note here that the results of our DFT measurements described in Sec. V, allow us to provide physical motivation for the origin of the canting and therefore further evidence that our model is appropriate.

Finally, the $[1,0,3-\tau]$ reflection was measured and an azimuthal dependence of the scattering collected. The structure factor for this reflection is dominated by the helical magnetic term, unless the phase difference between the orbits falls within the range 1.8 and 2.0 radians, canting strength dependent, in which case the canting component becomes the more dominant. Figure 8 shows the results of the azimuthal dependence of the $[1,0,3-\tau]$ satellite reflection. Three different models are shown in Fig. 8: the predicted azimuth for a circular helical structure with spins restricted within the a-b plane; a rotated elliptical structure; and the prediction using the c component only. The data does not agree quantitatively with any of the three models, while qualitatively it most resembles the elliptical model. The c component and circular models are significantly different from the measured result. This result

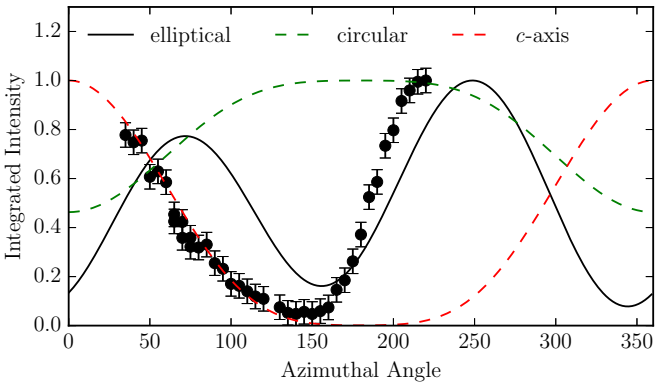

FIG. 8. Azimuthal measurement of the $[1,0,3-\tau]$ magnetic Bragg peak. The green dashed line shows the predicted azimuth for a circular helical magnetic structure. The black solid lines shows the prediction for an elliptical rotated magnetic structure. The red dashed line shows the results predicted using a magnetic helix pointing along the c axis. These predictions were calculated using the structure factors.

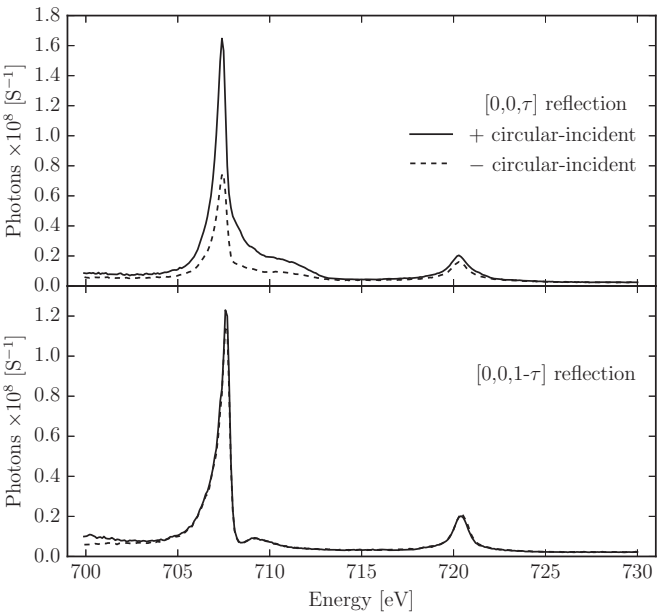

FIG. 9. Energy resonance of the magnetic satellite peaks, $[0,0,\tau]$ (top) and $[0,0,1-\tau]$ (bottom), with circular-positive and negative-polarized incident light.

is sufficient to further rule out the nonelliptical case, but the measurement is not sufficient to gain any information about the phase difference between the two orbits, nor the magnitude of the canting.

C. Determination of the chirality

The chirality of the magnetic structure has no effect on the simulations for a full linear polarization analysis, but is important when circular incident light is used [21]. For a chiral magnetic structure, incident circular positive and incident circular negative light can be used to establish the chirality [21].

Energy scans of the $[0,0,\tau]$ and $[0,0,1-\tau]$ reflections were performed at the Fe $L_{II/III}$ edges (Fig. 9). The predicted intensities of the $[0,0,\tau]$ and $[0,0,1-\tau]$ peaks were made using the structure factor calculations for both chiralities (Fig. 10). The intensity of the $[0,0,1-\tau]$ reflection does not change between circular positive and circular negative incident light, as this peak is sensitive only to the c-axis component that does not have a chiral nature. The $[0,0,\tau]$ peak does show a variation with incident circular light, and predictions show that one circular channel is expected to be over twice as intense as the other. This is observed to be the case. The predictions also show that for a right-handed chiral helix the positive circular channel is expected to be the most intense, and for a left-handed chiral helix the negative circular channel is expected to be more intense. The nonchiral case, where the two orbits have opposite chirality, is predicted to show equal intensity in the circular positive and negative channels. The energy scans show the positive circular channel was the most intense channel, ruling out the nonchiral case and strongly suggesting that the magnetic helix is right-handed.

As a check, the linear polarization analyzer was used to examine the scattered beam from the $[0,0,\tau]$ satellite

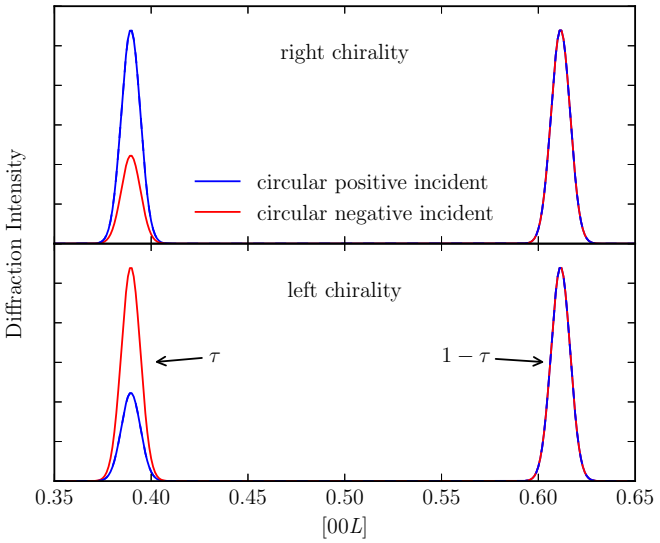

FIG. 10. Predicted intensities for circular incident polarization for the $[0,0,\tau]$ and $[0,0,1-\tau]$ for both right chiral (top) and left chiral (bottom) helical magnetic structure.

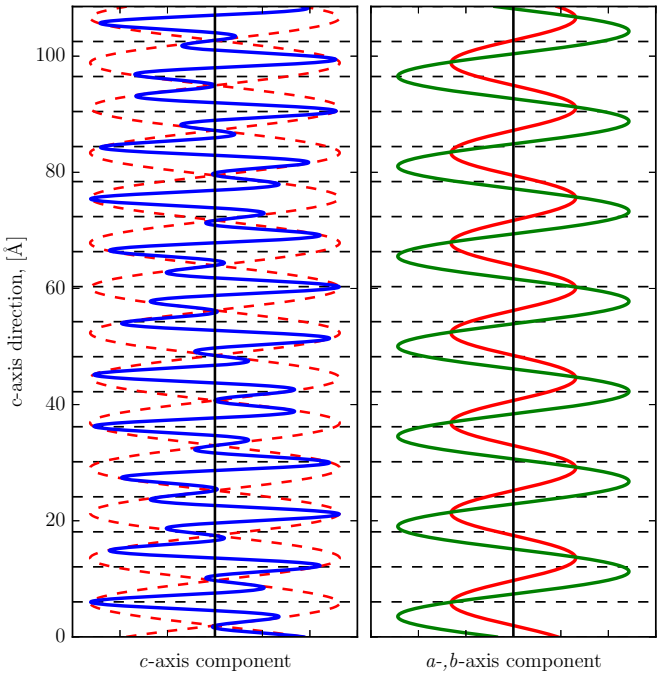

FIG. 11. a-, b-, and c-axis components of the magnetic helix, shown in red, green, and blue, respectively. The dashed red line shows the a-axis component envelope around the c-axis component.

reflection, with both circular positive and circular negative incident light. Using the helical structure factor, with the parameters from the fit of the linear polarization and azimuth measurements, the analyzer scans were simulated for both chiral cases. For the left- and right-handed chiral cases the positive and negative incident lights are predicted to show opposite behavior. We find that our measurement resembles the right-handed chiral structure, providing further confirmation that the magnetic helix has right-handed chirality.

The resonant x-ray scattering results have shown that a double circular helical magnetic structure is insufficient, and that the helix maps out an ellipse in the a-b plane. This ellipse has been shown to have an major axis 2.58 times longer than the minor axis. The azimuthal measurement showed that major axis of the ellipses is rotated -21° away from the b axis. The full polarization analysis of the unexpected $[0,0,1-\tau]$ peak, requires a canting of the a-axis component of the moment into the c direction with a periodicity of the unit cell. The absolute magnitude of the canting cannot be found from the measurements taken, just its presence. The phase difference between the two magnetic orbits has not been found. Figure 11 shows the a-, b-, and c-axis components of the magnetic moment for the canted spin helix, for one orbit.

This a-c canting relation, in which the a-axis component of the helix is canted with the periodicity of the unit cell c parameter, results in a total magnetic structure with a periodicity longer than given by τ. If we assign $\tau = 0.3\dot{8}$, such that the commensurate position is $\frac{7}{18}$, then the effect of the canting is to make the magnetic helix repeat every 18 unit cells along the c axis. This can be seen in Fig. 11 where the moment rotates around the helix seven times before returning to its starting position. It should be noted that we have assumed that the canting relation is between the a- and c-moment directions, as canting in the b direction would break the reflection symmetry. This unusual canting effect which only occurs along one direction of the helix combined with the ellipticity explains the unusual magnetic susceptibility measured by Segawa *et al.* [9]. While an elliptical helical structure goes some way to explain why the susceptibility along the b direction is lower than along the a direction, it does not explain the presence of the field splitting in only one direction.

V. DFT CALCULATIONS

Zero-spin DFT calculations on iron arsenide converged to a state with four bands crossing the Fermi surface, as shown in Fig. 12(a). Hole and electron curvature is present at the Fermi surface, in agreement with previous calculations and experiment [5,10]. No symmetry was enforced in the calculation and both the LDA and the GGA calculations converged onto a $Pnma$ symmetry.

Collinear spin-polarized calculations were performed for all spin parallel-antiparallel pairings in the unit cell. There are three antiferromagnetic states, a ferromagnetic state (FM), and a ferrimagnetic state where one spin is flipped from the FM state (FMSF). The antiferromagnetic states are identified by the iron atoms which have parallel spins: $Fe_1 \parallel Fe_3$ (AFM1), $Fe_1 \parallel Fe_4$ (AFM2), and $Fe_1 \parallel Fe_2$ (AFM3). The relative energies and ordered spin moment for these states and the zero-spin state using the GGA are shown in Table I. These agree with previous calculations [5]. The LDA results follow the same trends as the GGA results, but with lower ordered moments.

The magnitude of the ordered moment is found to increase with the number of antiferromagnetically aligned pairs of Fe moments. We also find that the energy of the states varies linearly with ordered moment. The energy relative to the AFM3 state is best fitted by $E = \gamma \sum_i |s_i| + \beta$, where the sum is over spins i, $\gamma = -74.8$ meV/μ_B, and $\beta = 394$ meV.

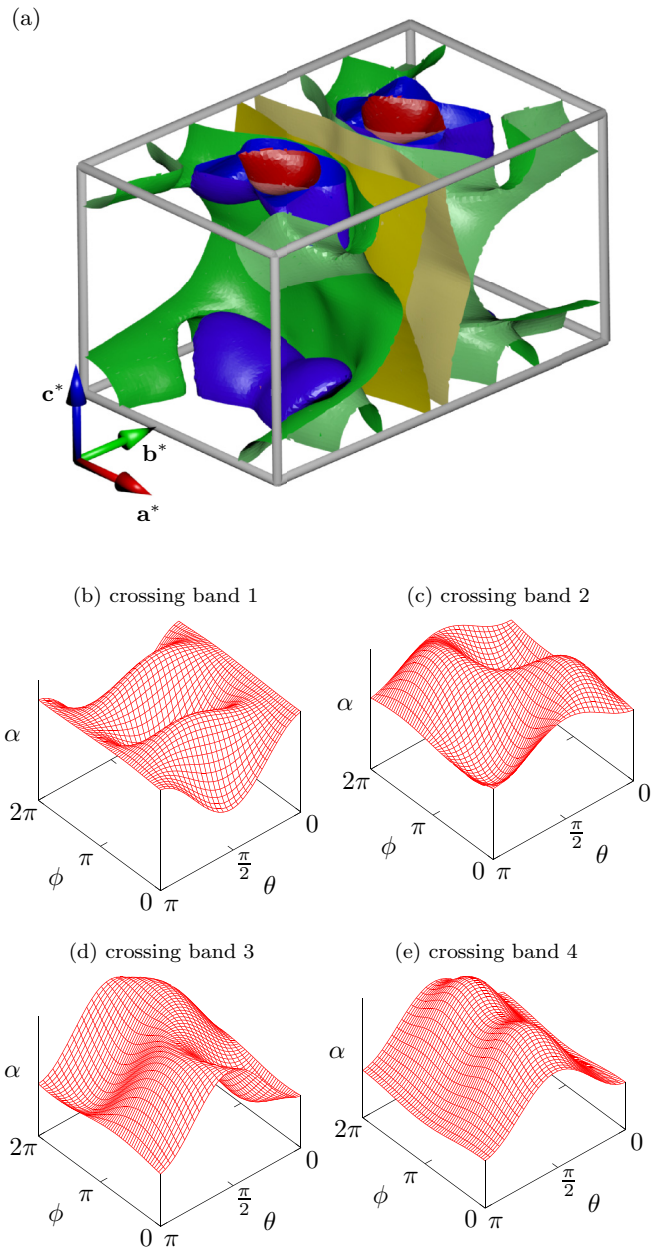

FIG. 12. (a) Fermi surface plot, (b–e) second-order spin-orbit perturbation energy α for each Fermi suface-crossing band, for different angular directions (θ,ϕ) of a Fe_1 probe spin. We use the Z-X-Z Euler angle conventions: θ is the angle away from c axis, ϕ is the angle away from b axis after projecting into the a-b plane. The axis coordinates (θ,ϕ) are given by $a = ((n + 1/2)\pi,(p + 1/2)\pi)$, $b = ((n + 1/2)\pi, p\pi)$, $c = (n\pi,\phi)$, with n and p integers.

TABLE I. Relative energies and spin magnitudes for different states calculated with the GGA, which show an almost linear relation between the two. *FMSF state has varying spin magnitudes, the mean value is stated here.

State	AFM1	AFM2	AFM3	FMSF	FM	zero-spin
Rel. energy meV/Fe	0	19	25	25	50	100
Spin mag. μ_B/Fe	1.32	1.06	1.00	0.98*	0.6	0

The observed linear energy dependence on spin magnitude contrasts sharply with the Heisenberg and Ising models, which have a quadratic energy dependence and is instead reminiscent of a Stoner instability as found in ferromagnetic metals [25]. Examination of the electron density in the system also shows that it changes with the transition to the ordered spin state. To explore the origin of this linear dependence we calculated differences in total electron density between states. Total density differences between the zero-spin state and AFM1 state are shown in Figs. 2(c) and 2(d). These show that when the system is relaxed into the AFM1 state, the electron density decreases between iron nearest neighbors (Fe_1-Fe_2, Fe_3-Fe_4) and increases along Fe-As bonds (Fe_n-As_n) in a pattern that forms strings along the a direction. The arsenic atoms were found to have a complicated local arrangement of spin density with no overall magnetic moment.

From our calculations we are able to provide an insight into the a-c canting relation of the magnetic order arises. The helical magnetic ordering wave vector is found to change with temperature [6], and this could imply that the system is sensitive to small perturbations. In fact, there are several frustrated nonequivalent Fe-As bonds in the material, which are likely to be responsible for the sensitivity of the ground state. There are three inequivalent Fe-Fe bonds, although one bond (Fe_1-Fe_3) is separated by a much larger distance than the others. We find that the spin moment magnitude on individual iron sites is correlated with the number of antiferromagnetically aligned nearest-neighbor Fe atoms. In our calculations, an iron atom with no antiferromagnetic short bonds has a moment of $0.6\mu_B$; those with two antiferromagnetic short bonds have a moment of $\approx 1\mu_B$, and those with all four antiferromagnetic short bonds have a magnitude of $1.32\ \mu_B$. In the lowest-energy state (AFM3), iron atoms linked by a long bond (Fe_1-Fe_3) must be ferromagnetically aligned. The trend in Table I shows that the structures with more antiferromagnetic bonds have a larger spin magnitude and lower total energy. An explanation for the occurrence of the helical magnetic state rather than AFM3 is that it allows the energetically unfavorable ferromagnetic pairing along the long bond in the AFM3 structure to reduce energy by canting.

Due to the sensitivity of the ground state, we expect weak mechanisms such as spin-orbit coupling to be decisive in realizing the ground state magnetic structure, and here we show that spin-orbit coupling explains the presence of the ordered component in the c direction. In order to see the effect of the spin orbit interaction on the ordered magnetic structure, we calculate the energetic perturbation of the spin-orbit interaction between the iron electron spins and the projected atomic orbitals. This is used to estimate the preferred direction of Fe spin alignment.

The perturbation to the ground-state energy can be calculated using the minimization of the energy density functional given by

$$H = H_0[\rho] + \varepsilon H_{\text{spin-orbit}}[\rho], \tag{5}$$

where $H_0[\rho]$ is our unperturbed density functional for the energy and ρ is the electron density. In the Kohn-Sham representation we can use the usual electronic formulation for the spin-orbit interaction, including it as a correction term to the electrostatic field around a given atom. This is

given by

$$H_{\text{spin-orbit}} = -\frac{\mu_B}{e\hbar c^2}\sum_{\Psi}\langle\Psi|\mathbf{s}\cdot\mathbf{L}\frac{dV}{dr_{\text{atom}}}\frac{1}{r_{\text{atom}}m}|\Psi\rangle, \quad (6)$$

where the sum is over the Kohn-Sham orbitals Ψ, V is the electrostatic potential around the atomic nucleus, r_{atom} is the distance to the center of the atom, and m is the band mass of the KS orbital. We approximate the electric field as radial, and this is valid as long as the core orbitals that shield the nuclear charge are not affected by the bonding. This radial symmetry leads to the condition $[\mathbf{L}, \frac{dV}{dr_{\text{atom}}}] = 0$, and further for FeAs we only consider the Fe $3d$ orbitals which are involved in the magnetic structure. This permits a significant simplification of the calculation.

For zero-spin calculations where $\rho_\uparrow = \rho_\downarrow$, the energetic perturbation α is second-order in the perturbation parameter [26] ε, and is given by

$$\alpha \propto -\varepsilon^2 \int \frac{|\langle\Psi|L_{z'}/m|\Psi\rangle|^2}{|\nabla U|}d\Psi, \quad (7)$$

where z' is the direction of the spin moment on an iron atom and $L_{z'}$ is the component of angular momentum in this direction. The integral is over the orbitals Ψ evaluated at the Fermi surface, and is dependent on the gradient of the energy U of the Kohn-Sham orbitals at the Fermi surface $|\nabla U(\Psi)|$. We find that the diamagnetic contribution of the orbitals is small compared to α and has therefore been neglected. A perturbation to the lowest nonzero order does not change the electron density from that of the ground state, and so we are free to choose the value of z' and calculate a physically meaningful energetic perturbation for this chosen spin orientation [27]. We are therefore able to create a full map of the energetic perturbation for different spin alignments. This allows us to assess the spin anisotropy of a specific Fe atom.

The principle parts of a plane-wave pseudopotential calculation are the projections of the Kohn-Sham orbitals onto the atomic basis set. The atomic orbital projections do not necessarily obey crystal symmetries. To generate the full set of projections the relevant local symmetry operators are calculated from the Wigner-d matrices [22] and, if required, the application of a reflection. From this complete orbital projection, projection amplitudes at the Fermi surface are calculated using a B-spline interpolation [23]. This projection of the Fermi surface is then used as the basis for the energetic perturbation computation.

The final result is calculated by applying Eq. (7) to each Fermi surface point, and $L_{z'}$ is calculated using a Mulliken orbital projection [24], and the use of Wigner-d matrices to include a rotation from the z direction to z' [22]. This is performed successively for each value of z' to generate a full map (in energy) of the perturbation, which is chosen to be a polar map with regular intervals in both θ and ϕ coordinates. We take the unperturbed state (corresponding to $H_0[\rho]$) to be the zero spin configuration. This state was chosen for the calculation as it has the largest Fermi surface. Results were obtained for an Fe_1 test spin aligned along different directions, and these energies are shown, for each band in Fig. 2. The calculations show clearly the effects of anisotropy, which causes a large difference in energy for different iron spin orientations. In general, we note that the extrema in energy do not lie along a crystal axis.

Crossing bands 3 and 4 (Fig. 2) makes a significantly larger contribution to α than the other bands, as they have the largest Fermi surfaces and the highest density of d orbitals. On band 3 the highest energy perturbation occurs when the Fe spin points in the a-c plane, at an angle of 23° from the c direction (toward a). We find that spin alignment along the b axis is energetically unfavorable. The results for band 3 compare favorably with the measured susceptibilities in the high temperature paramagnetic spin state, in which $\chi_a \approx \chi_c > \chi_b$ [9].

Finally, the anisotropy of the Fe d orbitals is calculated here from the second-order correction energy $\alpha(\theta,\phi)$ as $(1 - \alpha_{\text{min}}/\alpha_{\text{max}})$. This quantity, on band 3, is high in the a-c plane, at 81%, meaning that the local environment strongly affects the Fe d orbitals in this band. The other bands have anisotropies 77% (band 1), 51% (band 2), and 97% (band 4). For crossing band 2 the lowest energy spin direction lies exactly midway between a and $-c$; and in crossing band 4 it lies along c. The moment on the iron cannot satisfy all of these conditions simultaneously, but by far the largest proportion of d orbitals lie on crossing band 3. However, it is notable that the optimal direction of spin alignment lies off-axis in the a-c plane, and that spin-orbit effects will couple ordering in the a and c directions, with the relative orientation dependent on the iron site.

VI. CONCLUSIONS

In conclusion, we have used polarized resonant x-ray scattering measurements to investigate the incommensurate nature of the magnetic helix along the c axis in FeAs as well as its ellipticity. We have found evidence of a much greater ellipticity to that inferred previously, as well as a a-c canting relation in which moments are canted out of the a-b plane. In addition by use of circular polarized x-rays we have demonstrated the existence of a right-handed chiral structure. We have combined our experimental measurements with DFT calculations which have quantified the relative energies of different antiferromagnetic states and showed that the origin of the spin canting effect we have measured may be accounted for by considering the spin-orbit coupling. Finally, we note that the observation of both the fundamental magnetic satellite and also higher-order harmonics in FeAs suggest a different behavior to modulated antiferromagnetism in elemental metals such as chromium and the rare-earths.

ACKNOWLEDGMENTS

We are grateful to EPSRC and the John Templeton Foundation for financial support. We acknowledge Diamond Light Source for time on beamline I10 under proposal SI6422. Parts of this research were carried out using PO9 at the light source PETRA III at DESY, a member of the Helmholtz Association (HGF) (Grant No. I-20110275 EC). Work at King Fahd University of Petroleum and Minerals was supported by National Science Technology and Innovation Plan (NSTIP) under Project No. 11-ADV1631-04. We acknowledge the UK national supercomputing facility (Archer),

Durham HPC (Hamilton), the facilities of N8 HPC and the UKCP Consortium (EPSRC Grant No. EP/F037481/1). Data presented in this paper will be made available via doi.org/10.15128/r36h440s444.

[1] D. N. Basov and A. V. Chubukov, Nature Phys. **7**, 272 (2011).
[2] K. Ishida *et al.*, J. Phys. Soc. Jpn. **78**, 062001 (2009).
[3] M. R. Norman, Physics **1**, 21 (2008).
[4] S. Nandi, M. G. Kim, A. Kreyssig, R. M. Fernandes, D. K. Pratt, A. Thaler, N. Ni, S. L. Budko, P. C. Canfield, J. Schmalian, R. J. McQueeney, and A. I. Goldman, Phys. Rev. Lett. **104**, 057006 (2010).
[5] D. Parker and I. I. Mazin, Phys. Rev. B **83**, 180403 (2011).
[6] E. E. Rodriguez, C. Stock, K. L. Krycka, C. F. Majkrzak, P. Zajdel, K. Kirshenbaum, N. P. Butch, S. R. Saha, J. Paglione, and M. A. Green, Phys. Rev. B **83**, 134438 (2011).
[7] K. Selte and A. Kjekshus, Acta Chem. Scand. **23**, 2047 (1969).
[8] K. Selte, A. Kjekshus, and A. F. Andresen, Acta Chem. Scand. **26**, 3101 (1972)
[9] K. Segawa and Y. Ando, J. Phys. Soc. Jpn. **78**, 104720 (2009).
[10] B. Saparov, J. E. Mitchell, and A. S. Sefat, Supercond. Sci. Technol. **25**, 084016 (2012).
[11] S. M. Griffin and N. A. Spaldin, arXiv:1401.2277 (2014).
[12] S. M. Griffin and N. A. Spaldin, Phys. Rev. B **85**, 155126 (2012).
[13] K. A. Ziq, and A. F. J. Salem, Supercond. Nov. Magn. **26**, 1185 (2012).
[14] K. Lejaeghere *et al.*, Science **351**, 1415 (2016).
[15] S. J. Clark, M. D. Segall, C. J. Pickard, P. J. Hasnip, M. I. J. Probert, K. Refson, and M. C. Payne, Z. Kristallogr. **220**, 567 (2005).
[16] E. Fawcett, Rev. Mod. Phys. **60**, 209 (1988).
[17] L. M. Corliss, J. M. Hastings, and R. J. Weiss, Phys. Rev. Lett. **3**, 211 (1959); V. N. Bykov, V. S. Golovkin, N. V. Ageev, V. A. Levdik, and S. I. Vinogradov, Dokl. Akad. Nauk SSSR **128**, 1153 (1959) [Sov. Phys. Dokl. **128**, 1070 (1960)].
[18] Y. Tsunoda, M. Mori, N. Kunitomi, Y. Teraoka, and J. Kanamori, Solid State Commun. **14**, 287 (1974); J. P. Hill, G. Helgesen, and D. Gibbs, Phys. Rev. B **51**, 10336 (1995).
[19] M. Mori and Y. Tsunoda, J. Phys.: Condens. Matter **5**, L77 (1993); D. Lamago, M. Hoesch, M. Krisch, R. Heid, K.-P. Bohnen, P. Boni, and D. Reznik, Phys. Rev. B **82**, 195121 (2010).
[20] V. L. R. Jacques, E. Pinsolle, S. Ravy, G. Abramovici, and D. Le Bolloc'h, Phys. Rev. B **89**, 245127 (2014).
[21] A. M. Mulders, S. M. Lawrence, A. J. Princep, U. Staub, Y. Bodenthin, M. Garcia-Fernandez, M. Garganourakis, J. Hester, R. Macquart, and C. D. Ling, Phys. Rev. B **81**, 092405 (2010)
[22] E. P. Wigner, *Group Theory and Its Application to the Quantum Mechanics of Atomic Spectra* (Academic Press, New York, 1971).
[23] K. Esler, http://einspline.sourceforge.net/.
[24] R. S. Mulliken, J. Chem. Phys. **23**, 1833 (1955).
[25] E. C. Stoner, Rep. Prog. Phys. **11**, 43 (1947).
[26] J. J. Sakurai, *Modern Quantum Mechanics* (Addison-Wesley, Boston, 1985).
[27] J. F. Janak, Phys. Rev. B **18**, 7165 (1978).